# Mechanical and microstructural properties of a CoCrFe$_{0.75}$NiMo$_{0.3}$Nb$_{0.125}$ high-entropy alloy additively manufactured via cold-spray

David Funes Rojas[1], Haoyang Li[2], Okan K. Orhan[1], Chenwei Shao[3], James D. Hogan[2,*], Mauricio Ponga[1,*]

[1] Department of Mechanical Engineering, University of British Columbia, 2054 - 6250 Applied Science Lane, Vancouver, BC, V6T 1Z4, Canada

[2] Department of Mechanical Engineering, University of Alberta, Edmonton, AB T6G 2R3, Canada

[3] Laboratory of Fatigue and Fracture for Materials, Institute of Metal Research, Chinese Academy of Sciences, Shenyang 110016, People's Republic of China

## Abstract

We present a combined experimental and computational investigation of the mechanical properties of a CoCrFe$_{0.75}$NiMo$_{0.3}$Nb$_{0.125}$ (composition in molar ratio) high-entropy alloy additively manufactured via cold spray. We find that the sprayed alloy exhibits extraordinary mechanical properties under compression, reaching yield stress of $\sim$ 1745 MPa, ultimate stress of $\sim$ 2622 MPa, and a maximum strain at failure of $\sim$ 9%. These exceptional mechanical properties are the result of four independent hardening mechanisms. First, using *ab initio* simulations, we find that non-equiatomic compositions increase the enthalpy of mixing, promoting better solubility of solute Mo and Nb atoms while simultaneously preserving the electronegativity of the base alloy. The higher solubility results in solid-solution hardening and nanosized precipitate formation, promoting additional hardening. These effects are confirmed in the experimental characterization of the manufactured HEA, where nanosized precipitates of $\sim$ 226 $\pm$ 65 nm in size are identified. Additional hardening effects are associated with the manufacturing process, where the high-velocity impacts of the microparticles promote dynamic recrystallization through dislocation emission and grain refinement. To understand the dynamic recrystallization of particles, high-velocity impact simulations using molecular dynamics are performed. We find that when particles reach a critical impact velocity ($\sim 600 - 800$ m·s$^{-1}$), the dislocation density reaches a maximum, and grain refinement is maximized. The decaying wave pressures developed during the impact generate gradual refinement levels, leading to heterogeneous microstructures combining nano and micro grains, which was later confirmed experimentally using electron backscatter diffraction. These subtle atomic and microstructural features result in outstanding experimentally evaluated yield and ultimate stresses compared to other high-entropy alloys with similar compositions.

*Keywords:* High-entropy alloys, CoCrFe$_{0.75}$NiMo$_{0.3}$Nb$_{0.125}$, Cold-spray, Additive Manufacturing,

*Corresponding authors

*Email addresses:* `jdhogan@ualberta.ca` (James D. Hogan[2,*]), `mponga@mech.ubc.ca` (Mauricio Ponga[1,*])

## 1. Introduction

The quest for stronger materials with higher fracture toughness and better corrosion properties is a cornerstone in materials science and engineering [1]. In recent years, multi-principal element metallic alloys with near equiatomic proportions were introduced, challenging previous design concepts and leading rise to the *so-called* high-entropy alloys (HEAs) [2, 3]. Ever since these influential works, a large number of HEAs have been investigated due to their vast range of mechanical properties [4, 5], microstructural features [6], corrosion and high-temperature resistant qualities [7, 8]. HEAs challenge the design paradigm of traditional metallic alloys and thus, offer promising possibilities for the development of novel materials with remarkable mechanical properties [9].

HEAs primarily develop a single-phase crystalline structure due to several factors, among which the entropy and the enthalpy of mixing are thought to play a significant role in their thermodynamic stabilization [3]. Besides the large entropy of mixing, HEAs could result in heterogeneous microstructures where face-centered cubic (FCC) can coexist with body-centered cubic (BCC) and other intermetallic phases (see for instance Ref. [9] for a comprehensive database of HEAs). These possibilities open up a large spectrum for tailoring HEAs, making them an exciting system for diverse applications (e.g., in high-temperature applications, creep, corrosion environments [4–8]). Among all available systems, CoCrFeNi has been a popular choice at the center of many HEA designs. Most CoCrFeNi-based HEAs exhibit single FCC phase with non-chemical order [10], and have shown low yield strength ($\sigma_Y \sim 175$ MPa) with high ultimate strength and large failure strain (i.e., $\sigma_U \sim 472 - 2500$ MPa, at $\varepsilon_U \sim 60 - 75\%$) [11–18]. This low yield strength hinders the industrial application of HEAs, and thus, scientists have tried to develop hardening strategies, such as solid solution hardening (SSH) and precipitate hardening (PH), and used different manufacturing techniques to increase the mechanical performance of CoCrFeNi-based HEAs.

A common strategy for SSH is to use alloying elements with different radii as the base alloys. For instance, Liu *et al.* [18] and Shun *et al.* [19] have systematically investigated the effect of adding CoCrFeNiMo$_x$ with x = 0, 0.1, 0.2, 0.3, 0.5, 0.8[1]. They have found that increasing Mo results in an increment of the yield strength and a reduction of the failure strain. The increase in strength was attributed to SSH due to Mo additions and brittle and hard $\sigma$ and $\mu$ intermetallic compounds rich in Mo. Even more, thermal treatments can be used to achieve extraordinary mechanical properties ($\sigma_U = 1186$ MPa with a failure strain $\epsilon_p = 18.9$ %) [18]. Qin *et al.* [20] have also found that increasing Mo amounts can strengthen CoCrFeMnNi alloys due to the precipitation of $\sigma$ and $\mu$ intermetallic precipitates. Small additions of Mo can be used to extend the

---

[1]From now on, x values in molar ratio unless otherwise specified.

fatigue life of CoCrFeNi HEAs due to enhanced slip reversibility [21] which was attributed to lower stacking fault energy and higher elastic constants of the alloyed material. Li *et al.* [22] studied the fracture toughness of CoCrFeNiMo$_{0.2}$ HEA. They found that the addition of Mo increased the crack propagation resistance, but intermetallic phases rich in Cr of sizes between $1 - 3$ $\mu$m acted as stress concentrators and notches that promoted crack initiation and propagation. Thus, the interplay between intermetallic phases and solute atoms should be carefully evaluated when designing HEAs.

Other alloying elements, particularly Nb, have been investigated due to their different atomic radius. For instance, Liu *et al.* [23], and later He *et al.* [24], and Jiang *et al.* [25] have investigated the effect of Nb in the CoCrFeNiNb$_x$ system, with $x = 0.1 - 1.2$. These studies reported a substantial increase in the yield strength, albeit at the expense of reduced ductility due to Laves phases. Some of the investigated systems have shown failure strengths as high as 2479 MPa with a failure strain of 12.8%. Sunkari *et al.* [26] investigated a non-equiatomic CoCrFeNi$_{2.1}$Nb$_{0.2}$ HEA, and found excellent properties when it was cryo-rolled.

Besides conventional manufacturing methods, HEAs can also be manufactured using powder metallurgy (see Ref. [27] for a comprehensive review) making them potential candidates for additive techniques [28, 29]. Additive manufacturing (AM) techniques such as selective laser melting (SLM) [30], direct energy deposition (DED) [31], laser cladding [32], and sputter deposition [33] have also been recently explored to manufacture HEAs. AM methods are an appealing alternative to developing HEAs with complex and architected microstructure and geometries.

An appealing AM technique that allows the development of intricate microstructure is the *so-called* cold-spray (CS) technique. In CS, the feedstock material (i.e., metallic, ceramic, among other choices) is accelerated to high velocities through the use of a de Laval nozzle [34–36] and impacted onto a substrate. In contrast to other 3D techniques, the whole manufacturing process happens in solid-state in CS, and the adhesion is due to adiabatic shear instability [37–39]. As a result, cold-sprayed materials exhibit a large degree of recrystallization and residual dislocations, leading to complex mixtures of small and large grains to develop subtle microstructural features [37, 40–42]. This aspect of CS has been explored to achieve surface coatings that are ultra-resistant to corrosion and wear. CS can also be used in combination with other AM methods such as SLM, opening up a large spectrum of opportunities for manufacturing novel materials [43].

However, the use of CS in printing HEAs remains mainly unexplored besides the work of Yin *et al.* [44] being the very first one of using CS to manufacture a HEA. In their work, Yin *et al.* [44] have demonstrated the manufacturing of a FeCoNiCrMn HEA alloy with CS. They investigated the microstructural and tribological properties of the printed material and showed that the composition of the alloy was not changed due to the manufacturing process. Also, Yin *et al.* [44] found that the material shows a considerable level of recrystallization after the manufacturing process, resulting in a three-fold increase in the hardness of the material. However, deposition of HEA powders using CS remains largely unexplored.

Here, we report the mechanical and microstructural features of a $CoCrFe_{0.75}NiMo_{0.3}Nb_{0.1}$ cold-sprayed HEA. We found that the HEA showed outstanding mechanical properties under compression, achieving an overall yield strength of $\sigma_Y \sim 1745$ MPa, and ultimate strength of $\sigma_U \sim 2622$ MPa in quasi-static conditions while exhibiting about $\sim 10\%$ strain at failure. This behavior is attributed to a combination of alloy composition and manufacturing method, which are confirmed using a combination of scanning electron microscope (SEM) analysis, electron backscatter diffraction (EBSD), and X-ray diffraction (XRD) analysis, and atomistic simulations. Our study shows that HEAs can be manufactured with advanced printing techniques allowing to develop metallic alloys with tailored atomic (lattice), microstructural (grain size and morphology), and macroscopic (geometry) features.

## 2. Methodology

### 2.1. Material preparation

A nominal $CoCrFe_{0.75}NiMo_{0.3}Nb_{0.125}$ (corresponding to $Co_{24}Cr_{24}Fe_{18}Ni_{24}Mo_7Nb_3$ at%) HEA was manufactured by Sandvik Osprey LTD, UK. The HEA composition was informed using a series of *ab initio* simulations that are explained in the Supplementary information (**SI**) **Section 1.1**. In our design, Mo was added at the expense of reducing Fe by the same amount, while additions of Nb came from removing the remaining three base elements (Co, Cr, Ni) at the same proportions. The powder was gas atomized in nitrogen, obtaining particles with near-spherical shapes that were normally distributed with an average diameter $\phi = 38 \pm 7$ $\mu$m, shown Fig. 1a. A large percentage of these particles ($> 90\%$) were spherical with fewer particles with more irregular shapes, as shown in Fig. 1b. Extensive microscope characterization of the powder surface did not reveal dendritic structure as in other works [44]. Inductively coupled plasma optical emission spectroscopy (ICP-OES) was performed in the atomized particles to check their composition. The results of the analysis are shown in Table 1; it is evident that the alloy had a slightly higher percentage of Co and lower on Cr and Ni than the nominal one. Other elements such as Si (1.4 at%) and W (0.8 at%) appeared due to impurities in the manufacturing process. This level of impurities can appear due to the pre-mixed powders and their handling or during the gas atomization process, especially when the mixture is in the liquid phase where diffusion of the elements is fast. Contamination with previous mixtures or from the enclosure used to hold the liquid mixture are other possibilities.

Two plates of $70 \times 60 \times 9$ mm$^3$ (shown in Fig. 1c) were printed with the HEA powder under a nitrogen environment using the cold-spraying facilities of Impact Innovations GmbH, Germany. A printing pressure of 50 bar was used to print the material. Particle velocities between $600-800$ m·s$^{-1}$ and an operating particle temperature of $\sim 400 - 500$ °K were estimated with this pressure value, considering spherical particles of 30 $\mu$m in diameter and a density of 8300 kg·m$^{-3}$ [45]. A schematic view of the CS process is shown in Fig. 1d for completeness. The porosity of the printed HEA was investigated with a microCT scan (details in the
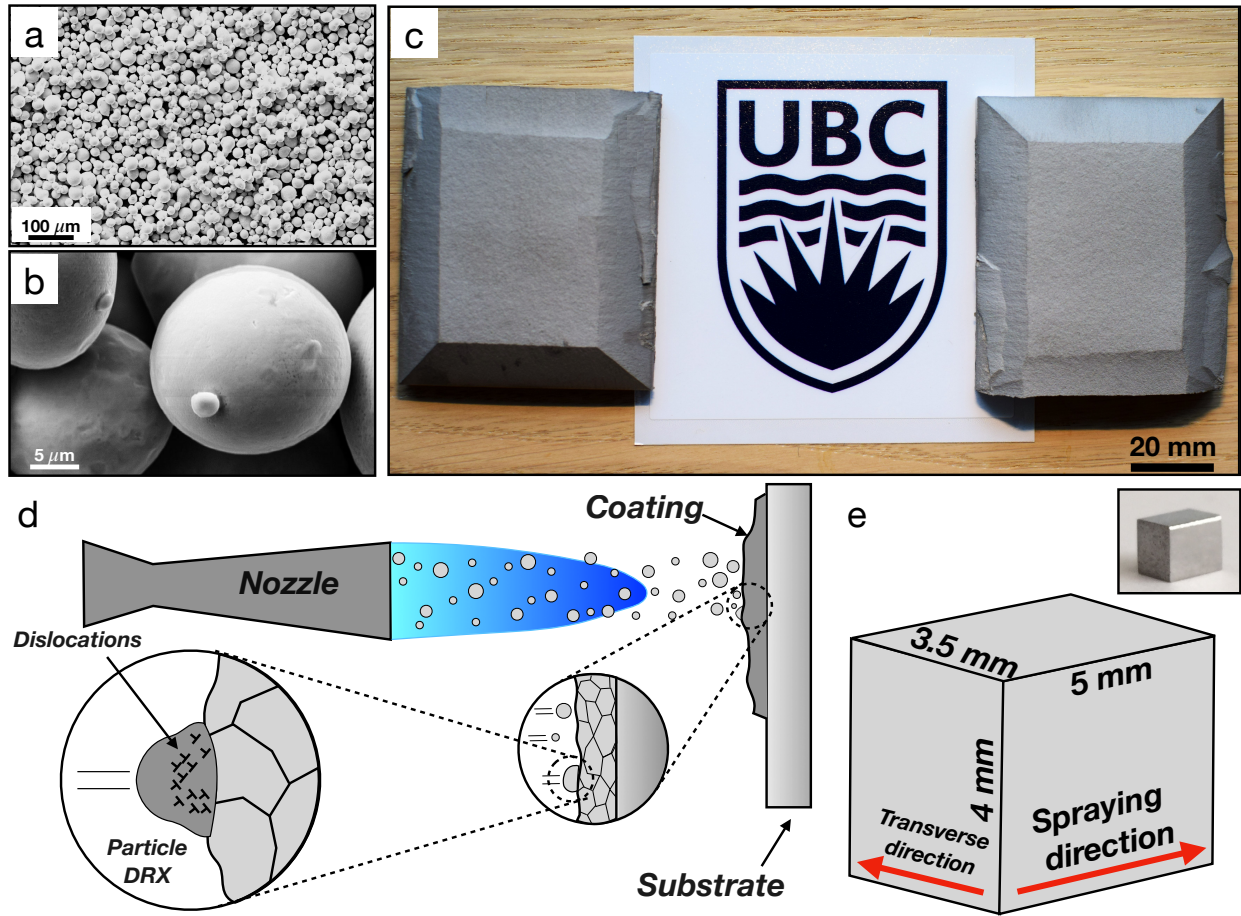
Figure 1: Cold-sprayed $Co_{24}Cr_{24}Fe_{18}Ni_{24}Mo_7Nb_3$ at% HEA (a) Atomized HEA powder of average diameter $\phi = 38$ $\mu$m. (b) Close-up view of the powder showing near-spherical particles. (c) View of the two printed specimens with dimensions $70 \times 60 \times 9$ mm$^3$. The HEA was sprayed over an Al 6061 substrate. (d) Shows the schematic cold spraying process, where a nozzle is used to accelerate particles that impact onto a substrate and generate the coating. Particle impact leads to large plastic deformation and dislocation emission, leading to dynamic recrystallization of grains. (e) Shows cuboidal samples (picture and schematic) with dimensions $5 \times 4 \times 3.5$ mm$^3$ made of the two sprayed plates. The printing direction is indicated.

Table 1: Composition of the HEA in powder and after the CS manufacturing process (at%). The powder analysis was carried out with Inductively Coupled Plasma Optical Emission spectroscopy (ICP-OES). The composition of the CS material was performed with an EDS sensor attached to the SEM. The values are obtained as the average of three scans along a polished and etched specimen.

| Element | Co | Cr | Fe | Ni | Mo | Nb | Si | W |
|---|---|---|---|---|---|---|---|---|
| Nominal | 24 | 24 | 18 | 24 | 7 | 3 | – | – |
| ICP-OES | 25 | 21.3 | 18 | 23.5 | 7 | 3 | 1.4 | 0.8 |
| EDS | 25.1 | 21.4 | 18 | 22.6 | 7.25 | 2.9 | 1.5 | 1.25 |

**SI Section 1.2**). The analysis revealed a good printing quality with only small voids well below 0.5% of porosity. After the CS manufacturing of the HEA, several cuboidal specimens were produced with electrical discharge machining (EDM), as shown in Fig. 1e. **Supplementary Video 1** shows the X-ray computer tomography scan in one of the specimens.

*2.2. XRD analysis*

The HEA powder was back-mounted as received in a Bruker cavity holder. Step-scan X-ray powder-diffraction data were collected over a $2\theta$ range of $20 - 120°$ with $CoK\alpha$ radiation on a Bruker D8 Advance Bragg-Brentano diffractometer equipped with a Fe filter foil, 0.6 mm (0.3°) divergence slit, incident- and diffracted-beam Soller slits, and a LynxEye-XE detector. The long fine-focus Co X-ray tube was operated at 35 kV and 40 mA, using a take-off angle of 6°. Sprayed specimens were also subjected to XRD analysis. XRD on HEA bulk specimen was carried out on a Rigaku XRD Ultima IV system with a $CuK\alpha$ beam source ($2\theta$ were subsequently converted to Co scale to be consistent with the powder data). The apparatus was operated at 40 kV and 44 mA on a standard stage. The phases were matched using the JADE software with the $K\alpha$ background signal removed.

*2.3. Microscopy details and mechanical testing*

Optical and scanning electron microscopes (SEM), Zeiss Sigma FESEM machine equipped both and energy-dispersive X-ray spectroscopy (EDS) and an electron backscatter diffraction (EBSD) detectors were used to characterize the particles. The SEM was operated with an acceleration voltage set at 20 kV with a working distance of $\sim 10$ mm. Micrographs were obtained using both *in-lens* and *secondary electrons* (SE) detectors. The EDS data was analyzed using the AZtec software from Oxford Instruments. SEM was utilized to study both printed material microstructures and post-mortem failure mechanisms, with EDS being used to confirm the element distribution after the printing technique. Grains were identified with EBSD using a misorientation angle greater than 3° from one pixel to the next.

Micro-hardness tests were performed using a Wilson VH1102 micro-hardness tester (Buehler Wilson, Illinois, USA) following the ASTM C1327 standard [46]. Mechanical compression tests were performed in the printed specimens using quasi-static compression tests utilizing a servo-hydraulic universal testing machine MTS 810 load frame [47]. Further details can be found in the **SI Section 1.3**.

## 3. Results

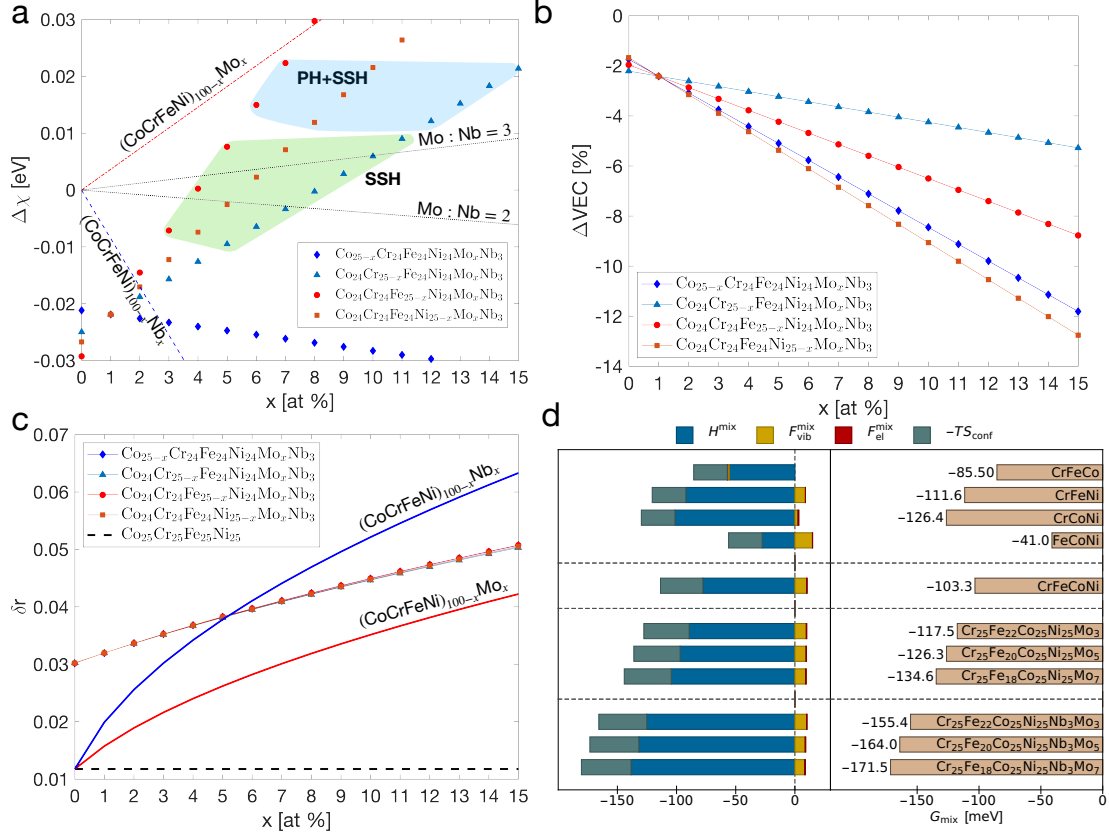### 3.1. Computational design of the HEA composition



Figure 2: Solid solution strategies for CoCrFeNi based HEAs. (a) Shows the change on electronegativity ($\Delta\chi$ in eV) for several alloys, including $(CoCrFeNi)_{100-x}Mo_x$ (dot-dashed line), $(CoCrFeNi)_{100-x}Nb_x$ (dashed line), $Co_{25-x}Cr_{24}Fe_{24}Ni_{24}Mo_xNb_3$ ($\diamond$), $Co_{24}Cr_{25-x}Fe_{24}Ni_{24}Mo_xNb_3$ ($\triangle$), $Co_{24}Cr_{24}Fe_{25-x}Ni_{24}Mo_xNb_3$ ($\circ$), and $Co_{24}Cr_{24}Fe_{24}Ni_{25-x}Mo_xNb_3$ ($\square$) at%. $\Delta\chi$ changes for $(CoCrFeNi)_{100-z}Mo_xNb_y$ at% with $z = x + y$ for ratios x/y=2 and 3 are also shown with labels Mo:Nb=2 and 3, respectively. Alloy compositions in the centrally shaded area have $\Delta\chi \sim 0$ and are potential candidates for SSH. Circled alloy compositions marked with PH+SSH could favor both SSH and PH. (b) $\Delta$VEC, (c) misfit parameter $\delta r$ for several compositions, and (d) mixing Gibbs free energies (right panel), and individual contribution to the Gibbs free energy (left panel) in meV units for several alloy compositions obtained with *ab initio* simulations. All HEAs compositions are shown in at%.

First, we describe the computational results used to inform the alloy selection process. We selected a

CoCrFeNi base alloy due to its small yield strength and large plastic deformation, and the substantial amount of work published using Mo or Nb [18, 19, 23–25]. However, the combination of using both elements at the same time has not been investigated as far as we are concerned. We started by evaluating several physical parameters of the base CoCrFeNi alloy, including its electronegativity ($\chi$), valence electron charge (VEC), average radius ($\bar{r}$), and misfit parameter $\delta r$ described in **SI Section 1.1**. We used *ab initio* simulations of the pure elements to compute the Mulliken electronegativity, which is commonly approximated as the negative of the chemical potential within the Kohn-Sham density-function theory (KS-DFT). Other parameters such as the atomic radii and valence electron charges were used and detailed in Table 2. Next, we examined two different strategies. First, we numerically investigated alloying with only one element (Mo or Nb) while reducing the proportions of the base elements equally. These results are shown in Fig. 2a with the label $(CoCrFeNi)_{100-x}Mo_x$, and $(CoCrFeNi)_{100-x}Nb_x$. Looking at the change of electronegativity ($\Delta\chi$), we observed that additions of Mo and Nb have opposite trends in $\Delta\chi$, where Mo results in higher $\chi$, while Nb leads to smaller $\chi$. We also observed that the magnitude of the slope of the $\Delta\chi$ plot is higher for Nb than Mo, suggesting that the ratio between Mo:Nb should be greater than one to avoid excessive differences in $\chi$.

Motivated by this findings, we investigated systems such as $(CoCrFeNi)_{100-z}Mo_xNb_y$ with z = x + y, while keeping the ratio of Mo:Nb to be two and three. The simulation results are shown in Fig. 2a labeled as Mo:Nb= 2/3. We observed that these combinations lead to small changes of $\chi$ compared to the base HEA. Since we wanted to promote high solubility and at the same time develop nanosized precipitates, we discarded these alloys because they could promote total solid solution of the solute elements in the base CoCrFeNi.

Thereafter, we adopted the following strategy where we combined Mo and Nb at the same time. We restricted our mixtures to a maximum of 10 at% for the solute atoms (both Mo and Nb) to avoid phase change and large precipitates [48].

Taking the ratio between Mo:Nb to be two and three, and keeping the solutes close to 10 at%, these two constraints restricted our design to the combinations of the pairs of Mo and Nb solute atoms of 6:3 and 7:3 at%, respectively. The addition of Nb was done at the expense of removing 1 at% of three principal base elements, while Mo additions were made by decreasing the remaining base element by the same amount. We have done this systematically for all four base elements, and the results are shown in Fig. 2a. Of particular interest, we found that additions of Mo at the expense of reducing Co resulted in increasing differences in $\chi$. This alloying strategy could lead to the preferential pairing of Mo with other base elements, resulting in complex intermetallic phases. Since we wanted to avoid such structures, we disregarded this possibility. We also noticed that alloys with low content of Cr and Ni lead to $\Delta\chi \sim 0$ which favors solid solution. These combinations are shown with a green area in Fig. 2a and marked as SSH. Furthermore, alloys with low Fe content had slightly higher $\Delta\chi$. In particular two alloys $Co_{24}Cr_{24}Fe_{19}Ni_{24}Mo_6Nb_3$ at%

8

and $Co_{24}Cr_{24}Fe_{18}Ni_{24}Mo_7Nb_3$ at% resulted in $\Delta\chi \sim 0.2$ eV (circled in Fig 2a marked with PS+SSH) while satisfying our constraint of solute atoms below 10 at%. Since our purpose was to develop both SSH and PH, we selected the latter as a potential candidate. $\Delta\chi \sim 0.2$ eV is an important figure of merit that can be used to design small precipitates in HEAs [18, 19, 23–25].

Looking at the remaining figures of merit, we observed that the studied compositions resulted in small reductions of the VEC as shown in Fig. 2b. This slight reduction is important since VEC can determine whether a HEA will result in pure FCC or mixed structures. Alloying with Mo and Nb results in a decrease of the VEC. This decrement was less than 8% when Mo is 7 at%. Thus, these small reductions of the VEC suggest that the FCC matrix of the alloy might be preserved for the alloyed systems. Looking at the misfit parameter $\delta r$, shown in Fig. 2c, we observed that the alloyed system resulted in a $\delta r = 4\%$, which will promote SSH but below the 6% critical misfit parameter [48].

Having decided on the alloying strategy, we investigated the proposed mixture's thermodynamics and compared it to the base HEA using further *ab initio* simulations. Preliminary simulations with three elements shown that the Gibbs free energy of mixing could change significantly depending on the combination of the elements, as shown in top left panel of Fig. 2d. The mixing free energy for the equiatomic four elements alloy is shown in the second panel from the top ($G_{mix}$(CrCoFeNi) = -103.3 meV per atom) and is used as a reference to compare with the alloyed mixtures. Next, we investigated the mixing Gibbs free energy for several systems, with increasing Mo while removing Fe, as shown in the third panel from the top of Fig. 2d. We see that addition of Mo results in an overall decrease of the mixing free energy, which further results in higher thermodynamic stability of the alloy. This decrement of the mixing energy is due to the enthalpy of mixing as opposed to an increment of the entropy, as shown in the left plots of Fig. 2d.

Table 2: Parameters for the elements that compose the cold-sprayed HEA. Radius of the elements in pm, $\chi$ is the Mulliken electronegativity in eV, and VEC is the valence-electron charge per volume for the elements (in $a_0^{-3}$). $\chi$ and VEC were obtained from *ab initio* simulations of the primary elements.

| Element | Co | Cr | Fe | Ni | Mo | Nb |
|---|---|---|---|---|---|---|
| Radius [pm] | 125 | 128 | 126 | 124 | 139 | 146 |
| $\chi$ [eV] | 8.126 | 7.746 | 7.318 | 7.573 | 8.056 | 6.841 |
| VEC [$a_0^{-3}$] | 0.129 | 0.077 | 0.104 | 0.136 | 0.054 | 0.041 |

We observed that the addition of both Mo and Nb increases the mixing energy even further compared to the addition of Mo alone, as shown in the bottom panel of Fig. 2d. These results suggest simultaneous additions of Mo and Nb to the base CoCrFeNi base HEA increase the thermodynamic stability of the alloy while preserving $\chi$ of the base alloy, which could lead to an increased solid solution of the alloying elements [20, 49].

## 3.2. XRD results

Figure 3 shows the XRD pattern for the HEA powder and cold sprayed specimen. Both powder and sprayed HEA exhibited a major FCC structure ($a_0 = 0.36052$ nm, and $\rho = 8354$ kg·m$^{-3}$) with well defined peaks. The lattice parameter is slightly higher than other CoCrFeNiMo$_x$ alloys ($a_0 = 0.3582$, $0.3599$ nm when x = 0.3 [18, 19]) and another with CoCrFeNiNb$_y$ ($a_0 = 0.3590$ nm when y = 0.103 [23]). Compared with the base alloy, the change in the lattice parameter was estimated to be 1.5%.

Additionally, two small peaks appear in the figure, left to the (111) peak. These peaks were located at $2\theta$ values that were a perfect match to the secondary ($\sigma$) phase identified by Shun *et al.* [19] (D8$_b$-type, $a = 0.9165$ nm, $c = 0.4739$ nm, and $c/a = 0.517$), and also identified by Liu *et al.* [18] in CoCrFeNiMo$_x$ when x = 0.3 (Mo $\sim$ 6.96 at%). These peaks did not correlate well with other phases identified in CoCrFeNi-based HEAs with similar Nb compositions. For instance, a close examination of Refs. [23, 24] where Laves phases were obtained indicated that the peaks of these intermetallic phases were placed at different angles compared to the one identified in this work. Furthermore, in CoCrFeNiNb$_x$ with low molar fraction of Nb, i.e., x = 0.103 (Nb $\sim$ 2.5 at%), Liu *et al.* identified a weak peak at around $2\theta = 51.5°$ but the location of the two peaks seen in our work are below 50° [23].

The XRD pattern showed peak broadening due to residual stresses developed during the manufacturing process. The microstrain in the sprayed alloy can be estimated with the XRD pattern with the Williamson-Hall method that was successfully applied to other HEAs [12, 50, 51]. The true peak broadening $\beta$ can be related to the microstrain in the specimen $\varepsilon_p$ and the crystallite size ($d$) as

$$\beta \cos \theta_B = \frac{\kappa \lambda}{d} + \varepsilon_p 4 \sin \theta_B, \tag{1}$$

where $\theta_B$ represents Bragg's angle of the peak, $\lambda$ is the wavelength of the Co K$_\alpha$ radiation source (0.179 nm), and $\kappa$ is a constant (0.9). The peaks' locations and magnitudes were automatically evaluated using the full width at half maximum algorithm in Matlab. Fitting these peaks to a linear plot, the slope of that fit represents a measure of the microstrain.

We evaluated this relationship for the four FCC peaks in the sprayed HEA; we obtained a microstrain $\varepsilon_p = 11 - 15\%$. Notice that the range of strain is quite wide since it depends on the fitting and large dispersion exists. Other studies have also identified large microstrain, i.e., $\varepsilon_p = 10.2\%$ in HEAs as well, supporting this analysis [51]. The crystallite size can be estimated using the first term in Eq. 1, which can be adjusted by fitting the data to a linear function. Using the HEA powder XRD pattern, we found that the crystallite size is $\sim 15$ $\mu$m. However, when the same analysis was carried out on the sprayed specimen it suggests grain refinement with an average size close to $\sim 0.14$ $\mu$m. These sizes were later confirmed in the microscopic characterization of the grains with EBSD discussed in the next section.
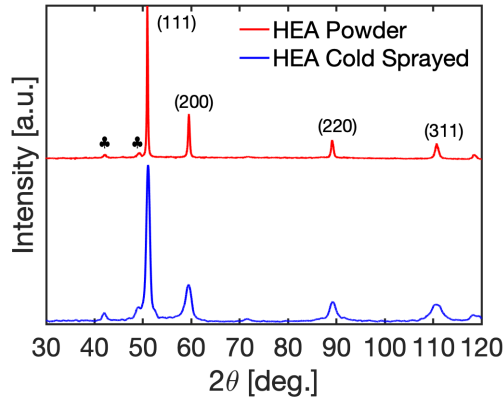
Figure 3: XRD diffraction pattern of the powder (top) and cold sprayed (bottom) HEA. The labels in the peaks denote specific FCC planes, while the ♣ symbol denotes the occurrence of intermetallic precipitates rich in Mo and Nb. The sprayed HEA shows peak broadening due to residual stresses developed during the manufacturing process.

### 3.3. Composition and microstructural analysis

Compositional analysis was carried out using ICP-OES and EDS. The composition using both methodologies, shown in Table 1, is in close agreement for both powder and sprayed specimens and close to the nominal alloy. Turning our attention to the spatial distribution of the elements, we observed that these elements were homogeneously distributed over the specimen, as shown in the EDS maps in **SI-Fig. 2**. Even though small composition variations were detected with EDS, the distribution of elements over the space is fairly homogenoeus.

Having studied the spatial composition of the alloy, we turn our attention to the microstructural analysis of the CS specimen. The summary of the microscopic investigations is shown in Fig. 4. We first observed that the CS specimens have a microstructure with grains of different sizes, as shown in Fig. 4a. Image analysis indicates that the average size of these visible boundaries is around $\sim 29$ $\mu$m with a standard deviation of $\sim 10$ $\mu$m, which compares well with the particle size of the powder. The smaller geometrical size (29 $\mu$m) compared to the original feedstock size (38 $\mu$m) supports the XRD findings that the particles suffered plastic deformation ($\varepsilon \sim 11-15\%$) during CS. We also observed that the shape of the grains is pretty regular, with most of the grains having the same length around the horizontal and vertical direction. Thus, there is a good correlation between the topology of the as-deposited grains and the feedstock.

The micrograph also illustrates interesting microstructural features of the sprayed specimen. The yellow arrows shown in Fig. 4a and b indicate the positions of several voids of different sizes. Two primary topological defects were observed, spherical and amorphous porous across the specimen. Spherical porous are the result of the printing process, where the impacting particles cannot fill up all the space. Amorphous porous are usually smaller than the spherical ones, and this can be seen in Fig. 4b, where a small crack of length $\sim 5$ $\mu$m can be observed (averaged over $\sim 50$ grains).
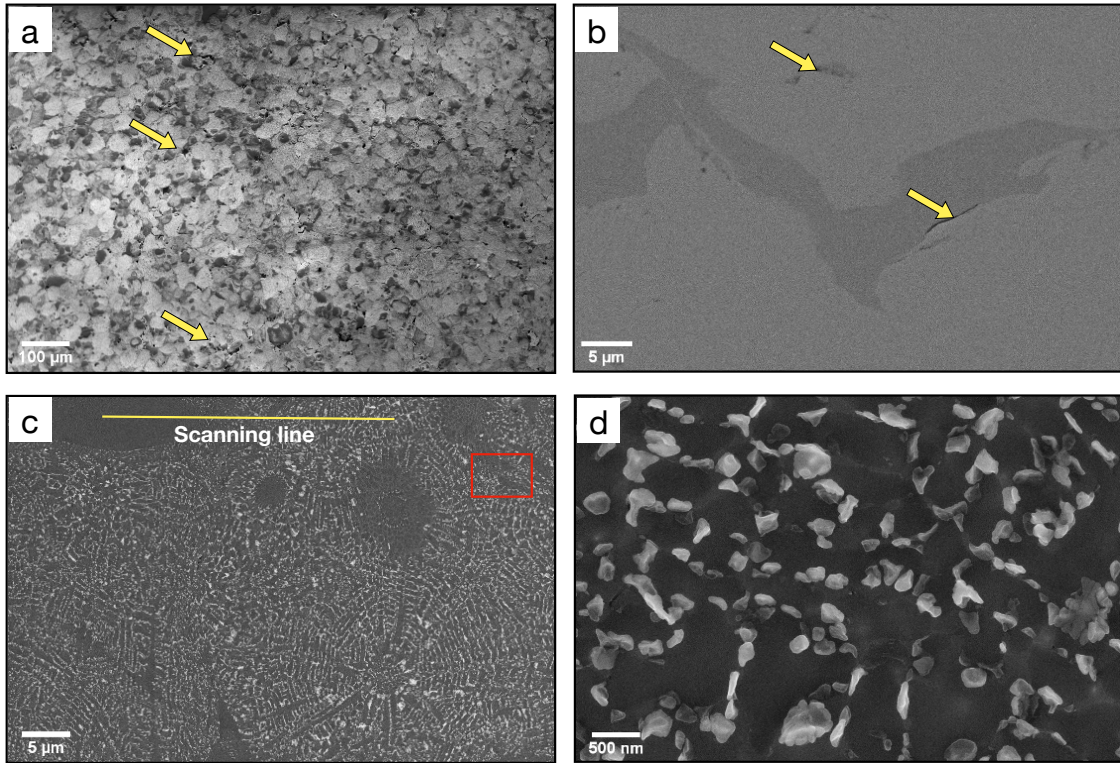
Figure 4: Microscopic characterization of the cold-sprayed HEA. (a) SEM view of the polished surface revealed the morphology of the printed particles. The boundaries seen correspond to the sprayed particles. The yellow arrows indicate the positions of porous defects in the sample. (b) Close up view of the printed specimen where a crack can be seen at the interface of two grains. (c) SEM view after electro-etched surface. The brighter regions indicate nanosized precipitates in the sample. Small grains can be also seen in the figure in areas where the precipitate density is low. The yellow line was used to scan with EDS the composition of the sample. The red box shown in the figure is the magnified in (d). (d) Close up view of the red area shown in (c) illustrating the size and morphology of the precipitates. We observed nano-sized precipitates of dimensions $\sim 226 \pm 65$ nm.

To gain more insights into the phases of the printed specimen, we electro–etched the specimen's surface for further microscopic analysis. The analysis showed nanosized precipitates homogeneously distributed across the specimen with the exception of some areas, as shown in Fig. 4c. Detailed microscopic analysis over areas where precipitate density was lower indicated presence of precipitates of slightly smaller size. This could possible be due the shock load developed during the impact and the posterior large plastic deformation experienced by the particles, which could reduce the precipitates size via dynamic recrystallization (DRX). Detailed microscopic analysis over the etched surface revealed the generation of smaller grains in addition to nanosized precipitates. These smaller grains are shown in areas where precipitates density was lower.

Measurement of grain size in these regions indicates a grain size between $100 - 200$ nm. Other areas showed a denser precipitate population, as shown in the red box in Fig. 4c. At higher magnification, the nanoprecipitate shapes can be seen in Fig. 4d. The analysis reveals that the precipitates are about $\sim 226 \pm 65$ nm in length, and the shape of these secondary phases can fluctuate between needle-like shape and almost spherical. A EDS line scan of the printed specimen performed over the yellow line shown in Fig. 4c (shown in **SI-Fig. 3**), revealed that the precipitates are rich in Mo (30% more than the fcc matrix) and Nb (45% more than the fcc matrix), with lower Co (20%), Fe (8%), and Ni (13%) content. Furthermore, the EDS line scan reveals that the impurities were homogeneously distributed in the matrix (see W distribution in **SI-Fig. 3**). The EDS scan shows that the impurities do not amalgamate at the nanosized precipitates regions nor form unique microstructural features in the material. Hence, we believe that Si and W do not contribute to additional failure mechanisms in the HEA.

To further confirm DRX of HEA particles during the CS process, we performed an EBSD scan in one of the samples along the sprayed direction on the $5 \times 3.5$ mm$^2$ face (see Fig. 1e). Fig. 5a shows an SEM image using the forescatter detector, which enhances topographic features of the microstructure. A scan of a $15 \times 15$ $\mu$m$^2$ area (shown in the red box in Fig. 5a) with high resolution ($\sim 40$ nm) is shown in Fig. 5b with the grains colored according to the inverse pole figure. We observed that the particles had undergone large plastic deformation, which, in turn, promotes dislocation emission and grain refinement and ultimately leading to DRX. This refinement was observed predominantly at the interfaces between particles due to the decaying wave pressures experienced during CS. At the intersection of the particles, the scanning failed to identify grains. This phenomenon is commonly observed in CS manufactured specimens due to void regions between the particles' interface or the large deformation of these areas, which could lead to very small grains and even disordered areas [37, 40].

A point-by-point Kikuchi band contrast is shown in Fig. 5c, where bright areas represent high crystallinity and dark areas indicate the opposite; this complements the picture of DRX in the particles. Analyzing the EBSD scan, we found that the grain size was much smaller than the particle size, with the averaged weighted fraction of the grain size shown in Fig. 5d. The inset in the figure shows all recognized grains colored with a different color. The average grain size was $d \sim 0.18$ $\mu$m (max 2.38 $\mu$m, min 0.09 $\mu$m) correlating well with the XRD analysis of the printed specimen (see Section 3.2). The pole figure of the scan is shown in Fig. 5e where the multiple of uniform distribution (MUD) is shown. Several peaks were observed in specific orientations and other areas where the distribution is close to homogeneous. These peaks correspond to the bulk of the particles, whereas the diffused distribution showed in green represents the recrystallized grains. As evident by the colormap the diffused green areas indicate that the nanosized grains are randomly oriented without any preferential orientation.

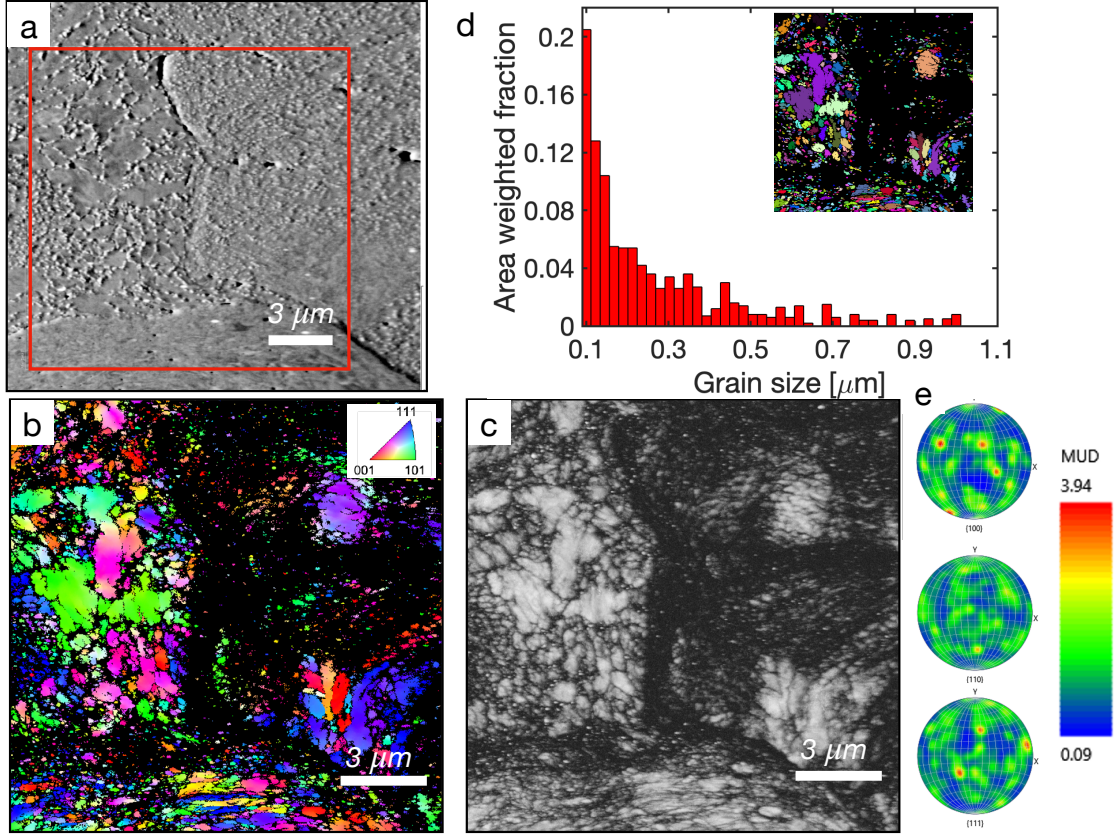To better understand the particle DRX during CS, we performed MD simulations closely following our

Figure 5: Grain identification in the CS-HEA with EBSD. (a) SEM figure over the printed face ($5 \times 3.5$ mm$^2$, see Fig. 1 for an interpretation of the different faces of the sample). The red box shows the area that was mapped ($15 \times 15$ $\mu$m) with the EBSD detector. (b) Grains identified with the EBSD detector and software. The grains are oriented according to the inverse pole inset at the top right. Several grains appeared due to recrystallization during the spraying process. Black dark areas represent sections where the algorithm could not identify the grain orientation due to severe distortion, or porosity. The white scale bar denotes 3 $\mu$m. (c) Point-by-point Kikuchi band contrast, where bright spots indicate high crystal quality and dark usually indicates surface damage or grain boundaries. (d) Grain size distribution in the scanned area, suggesting an average grain size of 0.18 $\mu$m, (max. 2.38 $\mu$m, min 0.09 $\mu$m). (e) Pole figure showing the grain orientation distribution in scanned area. The color scale indicates the multiple of uniform distribution (MUD). Perfect uniform (i.e., random) crystal orientation correspond to MUD=1 at all locations in the pole figure. The three figures represent the maps for the [1 0 0], [1 1 0], and [1 1 1] from top to bottom, respectively.

works on other FCC materials [52, 53] and detailed in the **SI Section 1.4**. MD simulations revealed that the plastic deformation and dislocation density reach an optimum for impact velocities between $v = 600 - 800$ m·s$^{-1}$ (see **SI-Fig. 4**), which is in close agreement with the estimated velocity during the spraying process. MD simulations also revealed DRX after the impact. Figures 6a-b show two cross-sections of the particles after impact where recrystallized grains have been assigned a unique color using an automatic segmentation algorithm [53]. We found several high-misorientation angle grains formed in the final microstructure, as
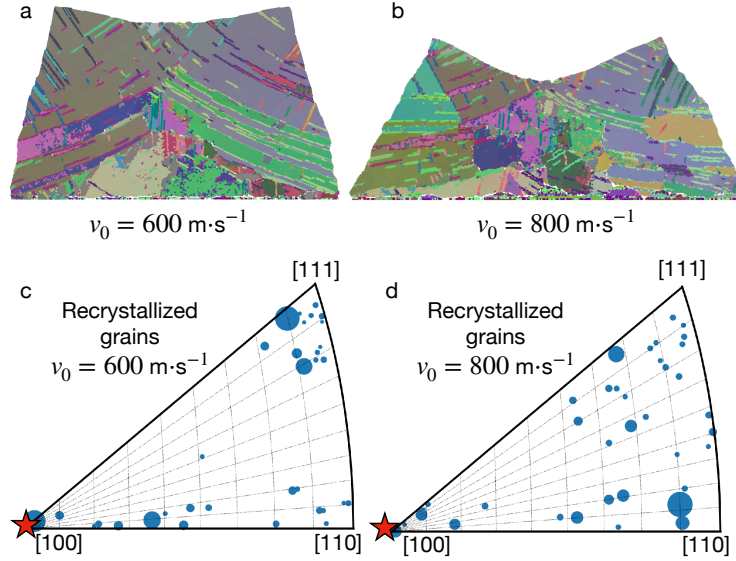
14

Figure 6: Dynamic recrystallization of HEA nanocubes impacting onto an impenetrable target of a particle at two different impact velocities (a) $v_0 = 600$ m·s$^{-1}$ and (b) $v_0 = 800$ m·s$^{-1}$. The different colors in the particle indicate different grains identified by the segmentation algorithm. Grains' orientation and size are shown below in the stereographic projections shown in (c) $v_0 = 600$ m·s$^{-1}$ and (d) $v_0 = 800$ m·s$^{-1}$. We observed that upon the impact, the particle has several grains with random orientations. These simulations explain the DRX of powder particles during the impact as observed in the microscopic analysis.

shown in the stereographic projections in Fig. 6c-d. Thus, the MD simulations provide the basis to support DRX during CS of HEA.

### 3.4. Mechanical properties of the cold-sprayed HEA

We now discuss the mechanical properties of the sprayed alloy. Microhardness measurements on the printing and transverse directions were $5.88 \pm 0.17$ and $6.40 \pm 0.20$ GPa, respectively. Uniaxial compression tests were performed using quasi-static loading. The engineering stress *vs.* strain plot is shown in Fig. 7. We see that the CS specimens show a monotonic hardening behavior. We also observed that the strain at failure is about $\varepsilon = 9\%$. Of tremendous interest, the yield stress, determined using the 0.2 % strain offset method, was $\sigma_Y = 1745$ MPa while the ultimate stress was in the neighborhood of $\sigma_U = 2622$ MPa (averaged over six successful tests). The elastic modulus, measured using the slope of the stress *vs.* strain plot was found to be $E = 146.8 \pm 3.6$ GPa. The mechanical properties of the CS HEA are detailed in Table 3 for completeness.

Further *in-situ* imaging of the specimen and DIC analysis revealed that the specimens, shown in the insets of Fig. 7a, developed a large shear band deformation zone where the strain concentrated. The shear band was approximately inclined about 45°, which is the orientation where the shear stresses are maximum in the uniaxially loaded specimens. While the global strain to failure is around 8.5-9 %, the deformation in the band can reach as high as 14 %, as can be seen in Fig. 7a for the last point. *Post mortem* examination

15

of the specimens revealed that cracks nucleate and propagate from the middle of the sample (see **SI-Fig. 5**).

Table 3: Mechanical properties of the cold-sprayed HEA. Density ($\rho_0$), yield strength ($\sigma_Y$), ultimate strength ($\sigma_U$), Young's modulus ($E$), Poisson's ratio ($\nu$), failure strain ($\varepsilon_U$), and Micro-hardness (mHV). Density is shown in kg·m$^{-3}$, stresses are given in MPa, Young's modulus in GPa, micro hardness measures are given in GPa. The values of micro hardness are given for the printing and transverse (in parenthesis) direction. For an interpretation of the directions see Fig. 1.

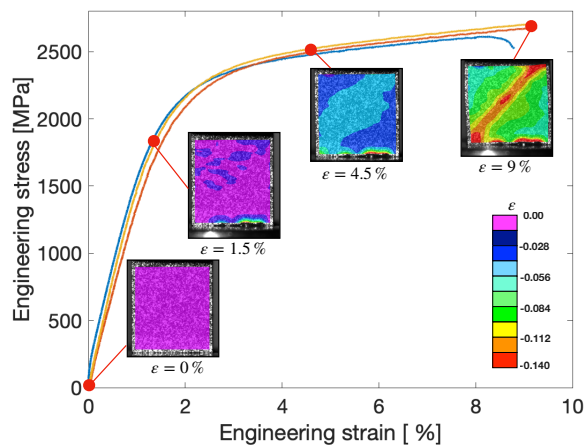| $\rho_0$ | $\sigma_Y$ | $\sigma_U$ | $E$ | $\nu$ | $\varepsilon_U$ | mHV |
|---|---|---|---|---|---|---|
| 8354 | 1745 | 2622 | $146.8 \pm 3.6$ | $0.26 \pm 0.018$ | 8.5-9.5% | 5.88 (6.40) |



Figure 7: Engineering stress *vs.* engineering strain behavior for the cold-sprayed HEA under quasi-static loading. Strain maps in one specimen at different engineering strains are shown in the insets. A shear band at approximately 45° can be observed before the failure of the specimen.

## 4. Discussions

The CS printing technique has been successfully applied to manufacture a CoCrFe$_{0.75}$NiMo$_{0.3}$Nb$_{0.125}$ HEA. Mechanical testing described in Section 3.4 indicated that the compressive yield stress of the sprayed specimen reached $\sigma_Y = 1745$ MPa, whereas the ultimate stress under compression rose to $\sigma_U = 2622$ MPa, and a strain at failure of $\varepsilon = 8.8\%$. These excellent mechanical properties under compression outperform other published results obtained for similar HEAs and, thus, are worth discussing why these differences appear. **SI-Table 1 and 2** show a summary of the published data on CoCrFeNi-based HEAs with additions of Mo and Nb. Figure 8 shows ultimate stress *vs.* failure strain for ease of comparison for tests under compression for several HEA compositions, i.e., CoCrFeNi [15, 16, 19, 25], CoCrFeNiY$_x$ (Y=Mo$_x$ [19], Nb$_x$ [24, 25], Cu [54], and Ti$_x$ [55]).
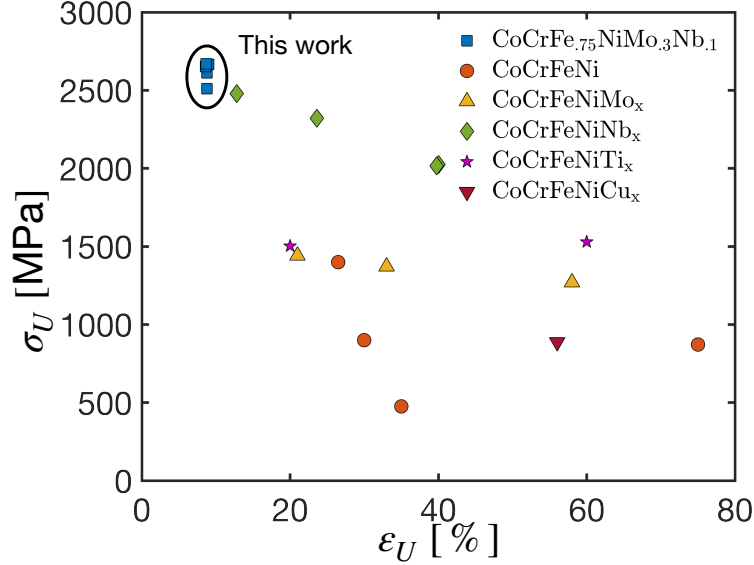
Figure 8: Comparison between ultimate stress ($\sigma_U$) and failure strain ($\varepsilon_U$) for different HEAs. Values were obtained only under compression tests from: CoCrFeNi [15, 16, 19, 25], CoCrFeNiMo$_x$ [19] and CoCrFeNiNb$_x$ [24, 25], CoCrCuFeNi [54] and CoCrFeNiTi$_x$ [55].

Shun *et al.* [19] investigated alloys with CoCrFeNiMo$_x$ with x = 0, 0.3, 0.5, 0.8 (Mo 0 at%, 7 at%, 11.1 at%, and 16.54 at%, respectively). They found that when Mo was increased to larger proportions, specifically to x = 0.8, their alloy showed an ultimate strengths of $\sigma_U$ = 1441 MPa with failure strain of 21% (plotted in Fig. 8 with $\triangle$ symbols). While the strength values reported by Shun *et al.* [19] are truly remarkable they are, however, below the ones obtained in our CS printed specimen. This observation reinforces our hypothesis that the Mo addition alone is not enough to achieve the strengthening in the CS alloy. Moreover, our alloy contained about Mo $\sim$ 7 at%, substantially lower than Shun *et al.* [19].

Next, we discuss the use of low content of Nb in our alloy. He *et al.* [24] investigated the effect of Nb in the CoCrFeNiNb$_x$ system, with x = 0.1 − 0.8 (Nb 2.5 − 16.65 at%, shown in Fig. 8 with $\lozenge$). He *et al.* [24] reported ultimate stress values ranging from 2025 to 2479 MPa, depending on the content of Nb. At the same time, they also observed a reduction of the fracture strain in the samples, from 38.8% to 12.8%. Remarkably, the alloy with the highest content of Nb (i.e., x = 0.8) showed a very close value of the ultimate stress to the sprayed alloy from the current study (cf. 2479 MPa to 2622 MPa). However, the amount of Nb in the sprayed alloy was considerably less (cf. x = 0.8 to x = 0.125). Jiang *et al.* [25] also investigated the CoCrFeNiNb$_x$ HEA system. They found that the ultimate strength increased to 2016 MPa by adding Nb x = 0.25 (Nb $\sim$ 6 at%) while achieving $\varepsilon_U$ = 39% (shown in Fig. 8 with $\lozenge$).

Next, we propose that the unusually high yield strength of the printed alloy is due to four factors that act independently. These factors include: (i) SSH due to the additions of Mo and Nb, (ii) second

hardening mechanisms is known as PH, where dislocation pin the precipitates found in our experimental characterization. Two additional hardening mechanisms associated with the manufacturing mechanisms are (iii) grain refinement due to dynamic recrystallization of the particles during CS and (iv) residual dislocations in the material. Below, we discuss each mechanism and provide an analytical basis to quantify them using models and theories.

### 4.1. Estimation of the solid solution hardening due to Mo and Nb additions

Toda-Caraballo [56] extended the earlier models proposed by Fleischer [57], Labush [58] for SSH in HEAs. Their approach to HEAs systematically evaluates the change of lattice parameter of the alloy w.r.t. the solute(s) content. The dependency of the hardening coefficient for each solute atom type $i$ is given by

$$B_i = 3\mu_{\text{HEA}}\epsilon_i^{4/3}Z, \quad \epsilon_i = \sqrt{\eta_i'^2 + (\alpha\delta_i)^2} \tag{2}$$

where $\mu = 58.25$ GPa is the shear modulus of the HEA computed through the relation $\mu = \frac{E}{2(1+\nu)}$, and

$$\eta_i' = \frac{\eta_i}{1 + 0.5|\eta_i|}, \quad \eta_i = \frac{\partial\mu}{\partial c_i}\frac{1}{\mu}, \quad \delta_i = \frac{\partial a}{\partial c_i}\frac{1}{a}, \tag{3}$$

where $\eta_i$ represents the dimensionless change of the shear modulus with respect to the concentration of the $i-$th solute, and $\delta_i$ represents the dimensionless change of the lattice parameter of the HEA with respect to the $i-$th solute. The former can be computed as

$$\eta_i = 2\frac{\mu_i - \mu_{\text{HEA}}}{\mu_i + \mu_{\text{HEA}}}. \tag{4}$$

Here, we rely on our *ab initio* simulations to compute the quantities in Eqs. 2 and 3. As stated by Toda-Caraballo, and Fleischer [56, 57], $\alpha$ is a parameter that accounts for the difference in the interaction forces between the screw and edge dislocations and the solute atom(s). Usually, $3 < \alpha < 16$ for screw dislocations, while $\alpha > 16$ for edge dislocations. Once the coefficients given above are computed, the increment of the yield strength is calculated using the following expression

$$\Delta\sigma^{\text{SSH}} = \left(\sum_i B_i^{3/2}c_i\right)^{2/3}. \tag{5}$$

We computed Eqs. 2-5 using *ab initio* simulations. These values are shown in **SI-Fig. 6** for several concentrations of Mo at%. We observed that with $Z^{-1} = 700$ a SSH of $\Delta\sigma^{\text{SSH}} = 40.25$ MPa and $\Delta\sigma^{\text{SSH}} = 115$ MPa for screw and edge dislocations are obtained when Mo 7 at%, and Nb 3 at%. Thus, while not negligible, the hardening achieved by SSH strategies represents a modest contribution in the sprayed alloy. These values seem to be close to the one reported experimentally but underpredicted the real strengthening. For instance, yield stress values reported by Liu and Shun and co-workers [18, 19] when Mo was added to the base alloy lead to $\Delta\sigma^{SSH} = 44 - 169$ MPa, while Liu *et al.* reported an increase in the yield strength of $\Delta\sigma^{SSH} = 170$ MPa for the alloy with similar content of Nb than ours.

## 4.2. Precipitation hardening in the HEA

To estimate the hardening due to precipitates, we invoke the model proposed by Bacon *et al.* [59], where precipitation hardening has been investigated. Briefly, the model proposes that the resolved critical shear stress required by dislocations to overcome microscopic precipitates and produce plastic deformation can be obtained as [59]

$$\tau^{\mathrm{PH}} = A\frac{\mu b}{L}\left[ \ln\left(\frac{\overline{D}}{r_0} + B\right)\right], \tag{6}$$

where $A = 1/2\pi$ for edge dislocations, whereas $A = 1/(2\pi(1-\nu))$ for screw dislocations, $r_0$ is the dislocation core size, $L$ is the mean distance between precipitates in the matrix, and $\overline{D} = (1/D + 1/L)^{-1}$ is an equivalent length that depends on the average precipitates' distance ($L$) and size ($D$). $B$ is a constant usually taken as 0.7 for normal precipitates size and distribution. For our alloy, all these parameters can be estimated using SEM and XRD characterization. We took $b = 0.255$ nm from the XRD analysis, $L = D = 226$ nm from the SEM characterization, and $\mu = 58.25$ GPa. The dislocation core size was estimated to be $r_0 = 3b$. Using these values, Eq. 6 gives a precipitation hardening of $\tau^{\mathrm{PH}} = 60$ MPa. Since in uniaxial compression testing, the maximum shearing stresses are half the principal normal stress, the increment in normal stress due to precipitates is $\Delta\sigma^{\mathrm{PH}} = 120$ MPa.

## 4.3. Dynamic recrystallization of particles

EBSD analysis of the sprayed sample revealed a complex microstructure with high levels of DRX in the particles. Furthermore, the EBSD map (see Fig. 5) indicated different levels of DRX of the grains, where nanosized grains were placed at the interface between particles, which is in close agreement with our MD simulation (see Fig. 6). We found that the average grain size was $d = 0.18$ $\mu$m (see Fig. 5d). Grain refinement is known to be a factor that contributes towards the hardening of materials via the Hall−Petch effect [60], which can be written as

$$\sigma_Y(d) = \sigma_0 + k_y d^{-1/2}, \tag{7}$$

where $\sigma_Y(d)$ is the yield strength due to the reduced grain size, $\sigma_0$ represents the yield strength for large grains, and $k_y$ is an experimentally adjusted constant that defines the importance of the Hall−Petch effect. For HEA, Liu *et al.* [60] have proposed $k_y = 226$ MPa·$\mu$m$^{1/2}$ for an equiatomic FeCoNiCrMn. Even though this is not the same composition we used in our work, we use this value to estimate the hardening due to grain refinement. This increment is $\Delta\sigma^{DRX} = 505$ MPa, which is more significant than the other two discussed mechanisms.

## 4.4. Residual dislocation hardening

The large amount of dislocation density produced due to the plastic deformation of the CS HEA could play an essential role in the overall hardening of the material. To estimate this contribution, we determined

the increment in hardening due to the residual dislocations as [61, 62]

$$\Delta\sigma^D = M\alpha\mu b\rho^{1/2}, \tag{8}$$

where $M = 3.06$ is a coefficient, $\alpha$ is a lattice dependent constant (0.2 for FCC materials), $\mu$ is the shear modulus, $b = 0.2549$ nm is the Burgers vector of the material, and $\rho$ is the residual dislocation density in the sample. The dislocation density can be obtained from the residual plastic strain, computed directly from the XRD pattern of the sprayed sample, and the crystallite size $d = 0.18$ $\mu$m as

$$\rho = \frac{2\sqrt{3}\varepsilon_p}{bd}. \tag{9}$$

Using the minimum estimated residual strain ($\varepsilon_p = 11\%$) obtained with the XRD pattern of the sprayed HEA, discussed in Section 3.2, we obtained an increment of the yield strength of $\Delta\sigma^D = 785$ MPa, while a maximum residual dislocation density of $\rho = 7.5 \times 10^{15}$ m$^{-2}$. Similar values for dislocation density were found in other HEAs that manufactured via spark plasma sintering, i.e., $\rho = 2.7 - 10 \times 10^{15}$ m$^{-2}$ [12]. This result is also in agreement with the dislocation density reported by Naeem *et al.* [63] in CrMnFeCoNi, where a peak value of $\sim 1 \times 10^{16}$ m$^{-2}$ was found at around 45% of deformation. Interestingly, Naeem *et al.* [63] reported that this value did not increase beyond this level and this behavior was attributed to the annihilation of dislocations [64].

Assuming that these four factors are independent, one can compute the total increment in hardening as the sum of all these contributions. The yield strength of the sprayed alloy can be estimated as

$$\sigma_y = \sigma_f + \Delta\sigma^{SSH} + \Delta\sigma^{PH} + \Delta\sigma^{DRX} + \Delta\sigma^D, \tag{10}$$

where $\sigma_f \sim 100$ MPa is the lattice friction contribution [65]. Solid solution hardening, precipitation hardening, grain, and dislocation hardening contributed 115, 120, 505, 785 MPa, respectively. These contributions total an overall yield strength of $\sim 1625$ MPa when the friction of the HEA was included. This value is not precisely the one obtained in our experimental testing but is very close. The discrepancies can be attributed to several factors, including approximations in the theories, errors in determining the dislocation density, and other factors such as the parameters used in the models, or the fact that SSH due to the impurities has not been considered. The effect of the impurities needs to be investigated further.

Nevertheless, the error between the averaged yield strength and the estimated one is less than 7%. Compared to grain boundary and dislocation hardening, solid solution and precipitation hardening play a modest role in the overall strength of the alloy. The high yield strength trade-off is the reduced strain at failure of the cold sprayed HEA specimens ($\varepsilon_U \sim 9\%$). The analysis suggests that thermal treatments can be employed to annihilate dislocations and anneal grain boundaries, resulting in smaller yield strength and increased failure strain [60]. This avenue could be explored to obtain a range of mechanical properties for cold sprayed HEAs.

## 5. Conclusions

In this work, we have investigated the mechanical properties of a cold-sprayed $CoCrFe_{0.75}NiMo_{0.3}Nb_{0.125}$ high entropy alloy. We found that the printed material had outstanding mechanical properties under compression, reaching an ultimate stress of $\sigma_U = 2622$ MPa. These properties are attributed to four independent mechanisms that act mutually to harden the material in which residual dislocation density and grain refinement are key players. Other mechanisms such as solid solution, precipitation hardening, and lattice friction play a modest role in this behavior. Both dislocation density and grain refinement are associated with the spraying process, which results in a mixed microstructure combining nano and micro grains.

Our work suggests a route to tailor mechanical properties of HEAs at different length scales, from the atomic composition to the microstructure, with the capability of developing complex three-dimensional shapes using additively manufacturing methods such as cold-spray. Future directions of this work could include the investigation of thermal treatments to reduce the sample's dislocation density to increase the maximum deformation to failure at the expense of reducing the alloy's strength and pursue other alloying strategies. Additionally, the tensile properties of the sprayed alloy remain unexplored, opening up a large spectrum of opportunities for future research. Some of these directions are actively pursued by the authors.

## 6. Acknowledgements

## References

[1] R. O. Ritchie. The conflicts between strength and toughness. *Nature Materials*, 10(11):817–822, 2011.

[2] B. Cantor, I. T. H. Chang, P. Knight, and A. J. B. Vincent. Microstructural development in equiatomic multicomponent alloys. *Materials Science and Engineering: A*, 375-377:213–218, 2004.

[3] J. W. Yeh, S. K. Chen, S. J. Lin, J. Y. Gan, T. S. Chin, T. T. Shun, C. H. Tsau, and S. Y. Chang. Nanostructured high-entropy alloys with multiple principal elements: Novel alloy design concepts and outcomes. *Advanced Engineering Materials*, 2004.

[4] M. H. Tsai and J. W. Yeh. High-entropy alloys: A critical review. *Materials Research Letters*, 2014.

[5] Z. Li, S. Zhao, R. O. Ritchie, and M. A. Meyers. Mechanical properties of high-entropy alloys with emphasis on face-centered cubic alloys, 2019.

[6] Y. Zhang, T. T. Zuo, Z. Tang, M. C. Gao, K. A. Dahmen, P. K. Liaw, and Z. P. Lu. Microstructures and properties of high-entropy alloys, 2014.

[7] Y. F. Ye, Q. Wang, J. Lu, C. T. Liu, and Y. Yang. High-entropy alloy: challenges and prospects, 2016.

[8] D B Miracle and O N Senkov. A critical review of high entropy alloys and related concepts. *Acta Materialia*, 122:448–511, 2017.

[9] S. Gorsse, M. H. Nguyen, O. N. Senkov, and D. B. Miracle. Database on the mechanical properties of high entropy alloys and complex concentrated alloys. *Data in Brief*, 21:2664–2678, dec 2018.

[10] M S Lucas, G B Wilks, L Mauger, J A Muñoz, O N Senkov, E Michel, J Horwath, S L Semiatin, M B Stone, D L Abernathy, and E Karapetrova. Absence of long-range chemical ordering in equimolar FeCoCrNi. *Applied Physics Letters*, 100(25):251907, 2012.

[11] Z Wu, H Bei, G M Pharr, and E P George. Temperature dependence of the mechanical properties of equiatomic solid solution alloys with face-centered cubic crystal structures. *Acta Materialia*, 81:428–441, 2014.

[12] Z. Fu, W. Chen, H. Wen, D. Zhang, Z. Chen, B. Zheng, Y. Zhou, and E. J. Lavernia. Microstructure and strengthening mechanisms in an FCC structured single-phase nanocrystalline Co25Ni25Fe25Al7.5Cu17.5 high-entropy alloy. *Acta Materialia*, 107:59–71, 2016.

[13] F. He, Z. Wang, Q. Wu, J. Li, J. Wang, and C. T. Liu. Phase separation of metastable CoCrFeNi high entropy alloy at intermediate temperatures. *Scripta Materialia*, 126:15–19, 2017.

[14] B. Wang, H. He, M. Naeem, S. Lan, S. Harjo, T. Kawasaki, Y. Nie, H. W. Kui, T. Ungár, D. Ma, and Others. Deformation of CoCrFeNi high entropy alloy at large strain. *Scripta Materialia*, 155:54–57, 2018.

[15] A. Zhang, J. Han, B. Su, P. Li, and J. Meng. Microstructure, mechanical properties and tribological performance of CoCrFeNi high entropy alloy matrix self-lubricating composite. *Materials & Design*, 114:253–263, 2017.

[16] J. Li, W. Jia, J. Wang, H. Kou, D. Zhang, and E. Beaugnon. Enhanced mechanical properties of a CoCrFeNi high entropy alloy by supercooling method. *Materials & Design*, 95:183–187, 2016.

[17] W. Huo, H. Zhou, F. Fang, X. Hu, Z. Xie, and J. Jiang. Strain-rate effect upon the tensile behavior of CoCrFeNi high-entropy alloys. *Materials Science and Engineering: A*, 689:366–369, 2017.

[18] W. H. Liu, Z. P. Lu, J. Y. He, J. H. Luan, Z. J. Wang, B. Liu, Y. Liu, M. W. Chen, and C. T. Liu. Ductile CoCrFeNiMox high entropy alloys strengthened by hard intermetallic phases. *Acta Materialia*, 116:332–342, 2016.

[19] T-T. Shun, L-Y. Chang, and M-H. Shiu. Microstructure and mechanical properties of multiprincipal component CoCrFeNiMox alloys. *Materials Characterization*, 70:63–67, 2012.

[20] G. Qin, R. Chen, H. Zheng, H. Fang, L. Wang, Y. Su, J. Guo, and H. Fu. Strengthening FCC-CoCrFeMnNi high entropy alloys by Mo addition. *Journal of Materials Science & Technology*, 35(4):578–583, 2019.

[21] Weipeng Li, Xiangyun Long, Shenghang Huang, Qihong Fang, and Chao Jiang. Elevated fatigue crack growth resistance of Mo alloyed CoCrFeNi high entropy alloys. *Engineering Fracture Mechanics*, 218:106579, 2019.

[22] W P Li, X G Wang, B Liu, Q H Fang, and C Jiang. Fracture mechanisms of a Mo alloyed CoCrFeNi high entropy alloy: In-situ SEM investigation. *Materials Science and Engineering: A*, 723:79–88, 2018.

[23] W. H. Liu, J. Y. He, H. L. Huang, H. Wang, Z. P. Lu, and C. T. Liu. Effects of Nb additions on the microstructure and mechanical property of CoCrFeNi high-entropy alloys. *Intermetallics*, 60:1–8, 2015.

[24] F. He, Z. Wang, P. Cheng, Q. Wang, J. Li, Y. Dang, J. Wang, and C. T. Liu. Designing eutectic high entropy alloys of CoCrFeNiNbx. *Journal of Alloys and Compounds*, 656:284–289, 2016.

[25] H. Jiang, L. Jiang, D. Qiao, Y. Lu, T. Wang, Z. Cao, and T. Li. Effect of Niobium on Microstructure and Properties of the CoCrFeNbxNi High Entropy Alloys. *Journal of Materials Science & Technology*, 33(7):712–717, 2017.

[26] U Sunkari, S R Reddy, B D S Rathod, S S Satheesh Kumar, R Saha, S Chatterjee, and P P Bhattacharjee. Heterogeneous precipitation mediated heterogeneous nanostructure enhances strength-ductility synergy in severely cryo-rolled and annealed CoCrFeNi2.1Nb0.2 high entropy alloy. *Scientific Reports*, 10(1):6056, 2020.

[27] J M Torralba, P Alvaredo, and Andrea García-Junceda. High-entropy alloys fabricated via powder metallurgy. A critical review. *Powder Metallurgy*, 62(2):84–114, 2019.

[28] Y. Brif, M. Thomas, and I. Todd. The use of high-entropy alloys in additive manufacturing. *Scripta Materialia*, 99:93–96, 2015.

[29] C. Han, Q. Fang, Y. Shi, S. B. Tor, C. K. Chua, and K. Zhou. Recent Advances on High-Entropy Alloys for 3D Printing. *Advanced Materials*, 32(26):1903855, 2020.

[30] R. Li, P. Niu, T. Yuan, P. Cao, C. Chen, and K. Zhou. Selective laser melting of an equiatomic CoCr-FeMnNi high-entropy alloy: Processability, non-equilibrium microstructure and mechanical property. *Journal of Alloys and Compounds*, 746:125–134, 2018.

[31] K. Zhou, J. Li, L. Wang, H. Yang, Z. Wang, and J. Wang. Direct laser deposited bulk CoCrFeNiNbx high entropy alloys. *Intermetallics*, 114:106592, 2019.

[32] Q. Chao, T. Guo, T. Jarvis, X. Wu, P. Hodgson, and D. Fabijanic. Direct laser deposition cladding of AlxCoCrFeNi high entropy alloys on a high-temperature stainless steel. *Surface and Coatings Technology*, 332:440–451, 2017.

[33] M. A. Tunes, V. M. Vishnyakov, and S. E. Donnelly. Synthesis and characterisation of high-entropy alloy thin films as candidates for coating nuclear fuel cladding alloys. *Thin Solid Films*, 649:115–120, 2018.

[34] A Moridi, S M Hassani-Gangaraj, M Guagliano, and M Dao. Cold spray coating: review of material systems and future perspectives. *Surface Engineering*, 30(6):369–395, 2014.

[35] W. Li, K. Yang, S. Yin, X. Yang, Y. Xu, and R. Lupoi. Solid-state additive manufacturing and repairing by cold spraying: A review. *Journal of Materials Science & Technology*, 34(3):440–457, 2018.

[36] S. Yin, P. Cavaliere, B. Aldwell, R. Jenkins, H. Liao, W. Li, and R. Lupoi. Cold spray additive manufacturing and repair: Fundamentals and applications. *Additive Manufacturing*, 21:628–650, 2018.

[37] H. Assadi, F. Gärtner, T. Stoltenhoff, and H. Kreye. Bonding mechanism in cold gas spraying. *Acta Materialia*, 51(15):4379–4394, 2003.

[38] M. Hassani, D. Veysset, V. K. Champagne, K. A. Nelson, and C. A. Schuh. Adiabatic shear instability is not necessary for adhesion in cold spray. *Acta Materialia*, 158:430–439, 2018.

[39] M. Hassani, D. Veysset, K. A. Nelson, and C. A. Schuh. In-situ observations of single micro-particle impact bonding. *Scripta Materialia*, 145:9–13, 2018.

[40] K. Kim, M. Watanabe, J. Kawakita, and S. Kuroda. Grain refinement in a single titanium powder particle impacted at high velocity. *Scripta Materialia*, 59(7):768–771, 2008.

[41] K. Kang, H. Park, G. Bae, and C. Lee. Microstructure and texture of Al coating during kinetic spraying and heat treatment. *Journal of Materials Science*, 47(9):4053–4061, 2012.

[42] M R Rokni, C A Widener, and V R Champagne. Microstructural Evolution of 6061 Aluminum Gas-Atomized Powder and High-Pressure Cold-Sprayed Deposition. *Journal of Thermal Spray Technology*, 23(3):514–524, 2014.

[43] S. Yin, X. Yan, R. Jenkins, C. Chen, M. Kazasidis, M. Liu, M. Kuang, and R. Lupoi. Hybrid additive manufacture of 316L stainless steel with cold spray and selective laser melting: Microstructure and mechanical properties. *Journal of Materials Processing Technology*, 273:116248, 2019.

[44] S. Yin, W. Li, B. Song, X. Yan, M. Kuang, Y. Xu, K. Wen, and R. Lupoi. Deposition of FeCoNi-CrMn high entropy alloy (HEA) coating via cold spraying. *Journal of Materials Science & Technology*, 35(6):1003–1007, 2019.

[45] K. Kim, S. Kuroda, M. Watanabe, R. Huang, H. Fukanuma, and H. Katanoda. Comparison of Oxidation and Microstructure of Warm-Sprayed and Cold-Sprayed Titanium Coatings. *Journal of Thermal Spray Technology*, 21(3):550–560, 2012.

[46] ASTM E92-82(2003)e2. Standard Test Method for Vickers Hardness of Metallic Materials. Technical report, ASTM International, West Conshohocken,, 2017.

[47] H Y Li, P Motamedi, and J D Hogan. Characterization and mechanical testing on novel $(\gamma + \alpha2)$ TiAl/Ti3Al/Al2O3 cermet. *Materials Science and Engineering: A*, 750:152–163, 2019.

[48] X Yang and Y Zhang. Prediction of high-entropy stabilized solid-solution in multi-component alloys. *Materials Chemistry and Physics*, 132(2):233–238, 2012.

[49] Y Wang, Z.-K. Liu, and L.-Q. Chen. Thermodynamic properties of {Al, Ni, NiAl, and Ni$_3$Al} from first-principles calculations. *Acta Materialia*, 52(9):2665–2671, 2004.

[50] G K Williamson and W H Hall. X-ray line broadening from filed aluminium and wolfram. *Acta Metallurgica*, 1(1):22–31, 1953.

[51] J Y He, H Wang, H L Huang, X D Xu, M W Chen, Y Wu, X J Liu, T G Nieh, K An, and Z P Lu. A precipitation-hardened high-entropy alloy with outstanding tensile properties. *Acta Materialia*, 102:187–196, 2016.

[52] R. Thevamaran, C. Griesbach, S. Yazdi, M. Ponga, H. Alimadadi, O. Lawal, S.-J. Jeon, and E.L. Thomas. Dynamic martensitic phase transformation in single-crystal silver microcubes. *Acta Materialia*, 182, 2020.

[53] D. F. Rojas, O. K. Orhan, and M. Ponga. Dynamic recrystallization of Silver nanocubes during high-velocity impacts. *Acta Materialia*, page 116892, 2021.

[54] X.F. Wang, Y. Zhang, Y. Qiao, and G.L. Chen. Novel microstructure and properties of multicomponent CoCrCuFeNiTix alloys. *Intermetallics*, 15(3):357–362, 2007.

[55] T-T. Shun, L-Y. Chang, and M-H. Shiu. Microstructures and mechanical properties of multiprincipal component CoCrFeNiTix alloys. *Materials Science and Engineering: A*, 556:170–174, 2012.

[56] I. Toda-Caraballo and P. E. J. Rivera-Díaz-del Castillo. Modelling solid solution hardening in high entropy alloys. *Acta Materialia*, 85:14–23, 2015.

[57] R L Fleischer. Substitutional solution hardening. *Acta Metallurgica*, 11(3):203–209, 1963.

[58] R Labusch. A Statistical Theory of Solid Solution Hardening. *Physica Status Solidi (b)*, 41(2):659–669, 1970.

[59] D J Bacon, U F Kocks, and R O Scattergood. The effect of dislocation self-interaction on the orowan stress. *The Philosophical Magazine: A Journal of Theoretical Experimental and Applied Physics*, 28(6):1241–1263, 1973.

[60] W H Liu, Y Wu, J Y He, T G Nieh, and Z P Lu. Grain growth and the Hall-Petch relationship in a high-entropy FeCrNiCoMn alloy. *Scripta Materialia*, 68(7):526–529, 2013.

[61] T. H. Courtney. *Mechanical behavior of materials*. Waveland Press, 2005.

[62] H. Wen, T. D. Topping, D. Isheim, D. N. Seidman, and E. J. Lavernia. Strengthening mechanisms in a high-strength bulk nanostructured Cu-Zn-Al alloy processed via cryomilling and spark plasma sintering. *Acta Materialia*, 61(8):2769–2782, 2013.

[63] M. Naeem, H. He, S. Harjo, T. Kawasaki, F. Zhang, B. Wang, S. Lan, Z. Wu, Y. Wu, Z. Lu, C. T. Liu, and X-L. Wang. Extremely high dislocation density and deformation pathway of crmnfeconi high entropy alloy at ultralow temperature. *Scripta Materialia*, 188:21–25, 2020.

[64] U. Essmann and H. Mughrabi. Annihilation of dislocations during tensile and cyclic deformation and limits of dislocation densities. *Philosophical Magazine A*, 40(6):731–756, 1979.

[65] Y.Y. Zhao and T.G. Nieh. Correlation between lattice distortion and friction stress in ni-based equiatomic alloys. *Intermetallics*, 86:45–50, 2017.